ARTICLE

Kinetic Analysis of Ag Particle Redispersion into ZSM-5 in the Presence of Coke Using *In Situ* XAFS

Received 00th January 20xx,
Accepted 00th January 20xx

DOI: 10.1039/x0xx00000x

Kazumasa Murata,[a] Junya Ohyama,[bc] and Atsushi Satsuma *[ac]

In the present study, the redispersion behavior of Ag particles on the ZSM-5 in the presence of coke was observed using *in situ* X-ray absorption fine structure (XAFS) spectroscopy. The dynamics of Ag particle redispersion into the ZSM-5 pores were evaluated by linear combination fitting (LCF) of the X-ray absorption near edge structure (XANES) spectra. In addition, the behavior of coke combustion in Ag-ZSM-5 was observed by thermogravimetric analysis (TGA). The rate constant of Ag particle redispersion was smaller than that of coke combustion at ≥500 °C, but it was three times larger than that of coke combustion at <500 °C. According to ^{27}Al magic angle spinning (MAS) nuclear magnetic resonance (NMR), the Ag^+ ions in the ZSM-5 pores improved the hydrothermal stability of Ag-ZSM-5. Therefore, a two-step regeneration process, in which the Ag particle redispersion proceeded first at low temperature (<500 °C) followed by a complete combustion of the coke at high temperature (≥500 °C) to prolong the catalyst lifetime.

1. Introduction

Aromatic compounds, such as benzene, toluene, and xylene (BTX), are generally used as solvents as well as raw materials for polymers and high value-added aromatic products. Typically, BTX is produced by catalytic reforming of heavy naphtha, which is derived from petroleum oil. However, petroleum oil is a finite carbon resource. Therefore, other resources for BTX are required. Recently, two methods have been spread for ethylene production: the dehydrogenation of ethane derived from shale gas and dehydration of ethanol derived from biomass. Therefore, ethylene aromatization was developed and implemented as an alternative BTX production. H^+-exchanged ZSM-5 (H-ZSM-5, MFI-type zeolite) was proposed as an effective catalyst for ethylene aromatization.[1–3] H^+ (Brønsted acid) site in H-ZSM-5 can efficiently activate ethylene. However, it shows low BTX selectivity due to the formation of aliphatic compounds. In order to improve the BTX selectivity, various metal-ion-exchanged ZSM-5 have been investigated.[4–7] Ag^+-exchanged ZSM-5 (Ag-ZSM-5) is a highly selective catalyst for aromatic compounds. Hsieh et al. reported that the ethylene aromatization through dehydrogenation and C–C bond formation synergistically proceeded between the H^+ and Ag^+ (Lewis acid) sites in Ag-ZSM-5.[8]

In addition, the zeolite catalyst may be deactivated by the deposition of coke formed during ethylene aromatization on its surface and inside its pores.[4,9–11] In general, the catalytic activities of zeolite catalysts are regenerated by coke combustion under oxidizing atmosphere (i.e., regeneration process).[12,13] However, H_2O produced during coke combustion causes dealumination and degradation of the zeolite framework.[13] Theoretical studies indicated that the dealumination of zeolite begins with the H_2O attacking the H^+ sites in zeolite.[14–17] Therefore, the exchange of H^+ sites in zeolite by metal ions is an effective strategy to improve its hydrothermal stability. It was reported that alkali metals, transition metals, and rare earth elements inhibit the dealumination of zeolite.[18–20] Ag^+ ions were also reported to enhance the hydrothermal stability of zeolite.[21,22] However, Ag^+ ions in ZSM-5 may be reduced to Ag particles under the reductive conditions of the ethylene aromatization reaction, which causes a significant deterioration in the catalytic performance.[22–24] In addition, the enhancement of the hydrothermal stability of ZSM-5 by Ag particles is probably not expected because the H^+ sites are formed with the formation of Ag particles. Typically, Ag clusters and Ag particles on zeolites or other oxides redisperse under an oxidizing atmosphere.[23,25–27] The rate of redispersion of Ag into Ag^+ ions compared to that of the coke combustion is an important factor to suppress the catalyst degradation. However, the kinetics of Ag particle redispersion and coke combustion are still not well understood, and the optimal regeneration conditions for Ag-ZSM-5 have not been established.

In this study, kinetic analysis was carried out for the redispersion of Ag particles into ZSM-5 in the presence of coke. The redispersion behavior was studied using *in situ* X-ray absorption fine structure (XAFS) spectroscopy and was indicated by linear combination fitting (LCF) of the X-ray absorption near edge structure (XANES) spectra. The effect of the regeneration conditions for Ag-ZSM-5 catalyst, i.e.,

[a] *Graduate School of Engineering, Nagoya University, Nagoya 464-8603, Japan. E-mail: satsuma@chembio.nagoya-u.ac.jp*
[b] *Faculty of Advanced Science and Technology, Kumamoto University, Kumamoto 860-8555, Japan.*
[c] *Elements Strategy Initiative for Catalysts and Batteries (ESICB), Kyoto University, Katsura, Kyoto 615-8520, Japan.*
Electronic Supplementary Information (ESI) available: [details of any supplementary information available should be included here]. See DOI: 10.1039/x0xx00000x

temperature (450–600 °C) and O_2 concentration (5%–15%), on the redispersion rate was also investigated. In addition, the coke combustion rate was estimated using thermogravimetric analyzer (TGA). To extend the lifetime of the Ag-ZSM-5 catalyst, a regeneration process was proposed based on the results of a comparison between the kinetics of the Ag redispersion and the coke combustion.

2. Experimental section

2.1. Catalyst preparation

H-ZSM-5 (Si/Al = 20, particle size = 10 μm) was obtained by the calcination of NH_4-ZSM-5 at 700 °C for 30 min. NH_4-ZSM-5 (840NHA) was purchased from Tosoh Co. Japan. Ag^+-exchanged ZSM-5 (Ag-ZSM-5, Ag/Al = 0.16, 0.37, and 0.51) was prepared using an ion-exchange method. The as-prepared H-ZSM-5 (H-ZSM-5-AP, AP: as-prepared, 4.5 g) was mixed with aqueous $AgNO_3$ (100 mL) at different concentrations (0.0125, 0.025, and 0.050 mol/L, respectively) in a 200-mL beaker under stirring at 45 °C for 2 h. The samples were then washed with distilled water (150 mL) for 30 min under continuous stirring at room temperature and filtered. The Ag^+ ion-exchange and washing process was repeated three times. The obtained sample was dried overnight at 80 °C and calcined at 550 °C for 4 h (denoted Ag-ZSM-5-AP, AP: as-prepared). Aromatized Ag-ZSM-5 (denoted Ag-ZSM-5-AA, AA: after aromatization) was prepared by exposing Ag-ZSM-5-AP to a flowing mixture of 50% C_2H_4/N_2 at 600 °C for 6 h. Regenerated Ag-ZSM-5 (denoted Ag-ZSM-5-AR, AR: after regeneration) was prepared by exposing Ag-ZSM-5-AA to a flowing mixture of 10% O_2/N_2 at 450 °C for 16 h and then at 600 °C for 2 h. Ag-ZSM-5 containing Ag particles in the absence of coke deposition prepared by H_2 reduction at 600 °C under a flowing mixture of 50% H_2/N_2 for 1 h (denoted Ag-ZSM-5-AH, AH: after H_2 reduction). Ag-ZSM-O (O: after oxidation) was prepared by exposing Ag-ZSM-5-AP to a flowing mixture of 10% O_2/N_2 at 600 °C for 1 h. To investigate the hydrothermal stability, H-ZSM-5-AP and Ag-ZSM-5-AP samples were hydrothermally treated at 700 °C under a flowing mixture of 3% H_2O/N_2 for 16 h (denoted H-ZSM-5-HT and Ag-ZSM-5-HT, respectively).

2.2. Inductively coupled plasma emission spectroscopy (ICP)

The loading weight of Ag in the Ag-ZSM-5 was investigated by an ICP spectrometer (SPS7800, Seiko Instruments Inc.). Ag-ZSM-5-AP powder was dissolved using hydrofluoric acid, which was then completely evaporated by heating a Teflon beaker at 80 °C. The resulting solution was diluted to a total volume of 50 mL using distilled water.

2.3. Temperature programmed desorption of NH_3 (NH_3-TPD)

To evaluate the acid properties of H-ZSM-5 and Ag-ZSM-5, NH_3-TPD was conducted using a BELCAT-Ⅱ (MicrotracBEL) with thermal conductivity detector (TCD). Samples (50 mg) were pretreated under 20% O_2/Ar for 30 min at 500 °C. When the temperature decreased to 100 °C, NH_3 adsorbed on H-ZSM-5 and Ag-ZSM-5. The adsorbed NH_3 was purged under He at 100 °C, and the temperature was then increased to 700 °C at 10 °C/min under He.

2.4. X-ray diffraction (XRD) measurements

The XRD measurements were carried out using a Rigaku MiniFlex II/AP diffractometer with Cu Kα radiation.

2.5. XAFS measurement

Ag K-edge XAFS measurement was carried out in a transmission mode at the BL14B2 beamline of the SPring-8 synchrotron radiation facility of the Japan Synchrotron Radiation Research Institute in Hyogo, Japan. The photon intensity and the beam size on the sample were ~10^{10} photons s^{-1} and 5 mm (horizontal) × 1 mm (vertical), respectively. XAFS spectra were collected in transmission mode in 25400–26200 eV range using a Si(311) double crystal monochromator with a Rh focusing mirror at 1.8 mrad and by using ionization chambers. The *ex situ* XAFS was performed at room temperature. For *in situ* XAFS, Ag-ZSM-5-AA (200 mg) was pressed using hands into a 7-mm diameter pellet for the gas diffusion and placed in a quartz cell (its volume; 104 mL) connected to a gas flow system (Figures S1 and S2). A mass spectrometer (Pfeiffer Vacuum) was used to monitor the eluent gas. In order to observe the behavior of Ag redispersion, the sample was preheated from room temperature to *X* °C (*X*=450, 500, 550, and 600) at a heating rate of 10 °C min^{-1} under He and then was exposed to a flowing of *Y*% O_2/He (*Y*=5, 10, and 15) at a flow rate of 100 mL min^{-1} at *X* °C. *In situ* XAFS measurements were performed at 1 min intervals once the oxygen was introduced in the glass cell. The experiment profile of the *in situ* XAFS is shown in Figure S3. The data analysis was performed using the Athena and Artemis software included in the Demeter package.[28] The *ex situ* extended X-ray absorption fine structure (EXAFS) spectra in *k* space were obtained within Fourier transformations (FTs) ranges of 3.0–11.0 $Å^{-1}$. Curve fitting analyses of FTs of EXAFS were performed in *R*-space between 1.0 and 3.2 Å. The signal-to-noise ratios of the *in situ* EXAFS spectra were not good because the *in situ* XAFS spectra were measured at higher temperatures than 450 °C. Therefore, *in situ* EXAFS spectra were performed FTs in the narrow range of 3–7 $Å^{-1}$.

2.6. TGA measurement

The combustion test of coke in Ag-ZSM-5-AA was carried out using TGA (Rigaku Thermo plus EVO2). The sample (about 10 mg) was placed into an alumina pan and preheated from room temperature to *A* °C (*A*=400, 450, 500, 550, and 600) at a heating rate of 10 °C min^{-1} under Ar. It was then subjected to a flow of *B*% O_2/Ar (*B*=1, 5, 10, 15) at a flow rate of 100 mL min^{-1} at *A* °C (*A:* as mentioned above).

2.7. ^{27}Al magic angle spinning (MAS) nuclear magnetic resonance (NMR)

^{27}Al MAS NMR analysis was performed on a JNM-ESCA 700 MHz NMR spectrometer (JEOL) operating at a magnetic field of 16.4

T and an ^{27}Al Larmor frequency of 182.43 MHz. All tests were performed at a sample spinning rate of ~15 kHz. A single pulse sequence with a pulse width of 0.6 μs, which corresponds to a pulse angle of ~30°, was used. Each spectrum was acquired based on 512 scans with a recycle delay time of 2 s and an acquisition time of 11.2 ms. All spectra were externally referenced to $AlK(SO_4)_2{\cdot}12H_2O$ (0 ppm). Asymmetric NMR peaks were fitted using two or more Gaussian peaks because ^{27}Al have quadrupole moment and Al atoms in ZSM-5 were slightly different.

3. Results and discussion

3.1. Physicochemical properties of Ag-ZSM-5

The Ag/Al ratios of the three Ag-ZSM-5-AP samples, which were ion-exchanged at three different concentrations of $AgNO_3$ aqueous solutions, were determined by ICP analysis to be Ag/Al = 0.16, 0.37, and 0.51 with Ag loading of 1.5, 3.3, and 4.5 wt%, respectively. Figure S4 shows the UV-vis spectra of H-ZSM-5-AP and Ag-ZSM-5-AP samples with different Ag/Al ratios. The intensity of UV absorption bands between 200 and 250 nm attributed to $4d^{10}$ to $4d^95s^1$ transition of isolated Ag^+ ion increased with increasing the Ag/Al ratio.[23,24,29,30] On the other hand, no band derived from Ag clusters (ca. 250–330 nm) or large Ag particles (ca. 330–500 nm) were detected. Thus, the UV-vis spectra showed that only Ag^+ ions were present in Ag-ZSM-5-AP.

Figure S5 shows the NH_3-TPD profiles of H-ZSM-5-AP and Ag-ZSM-5-AP samples with different Ag/Al ratios. H-ZSM-5 showed two NH_3 desorption peaks at low (200 °C) and high (430 °C) temperatures. The peak at 200 °C was attributed to the NH_3 species adsorbed on the weak acid site or physically adsorbed NH_3 species on H-ZSM-5. The peak at 430 °C was attributed to the NH_3 species adsorbed on the Brønsted acid site of the bridged Si–OH–Al in the zeolite frameworks.[31–33] On the other hand, the two desorption peaks of Ag-ZSM-5-AP appeared at higher temperatures compared to that of H-ZSM-5-AP. This result demonstrates the present of stronger Lewis and Brønsted acid sites by the introducing Ag^+ species.[34,35] The desorption peak at 250 °C was attributed to Ag^+ Lewis acid sites.[36] The desorption peak at 550 °C can be interpreted to the enhanced Brønsted acid by the interaction between the Ag^+ ions and Brønsted acid.[37] Moreover, Figure S6 shows IR spectra of H-ZSM-5 and Ag-ZSM-5-AP samples with different Ag/Al ratios in the OH stretching vibration region (3000–4000 cm^{-1}). The IR bands at 3600, 3654, and 3735 cm^{-1} were attributed to the Brønsted acid site of the bridged Si–OH–Al, acidic OH group located on extra-framework Al species, and silanol groups, respectively. As Ag/Al ratio increased, the IR band at 3600 cm^{-1}, which was derived from the bridged Si–OH–Al in zeolite, decreased. These proves that the Ag species in Ag-ZSM-5-AP are coordinated to the bridged Si–O–Al as Ag^+ ions.

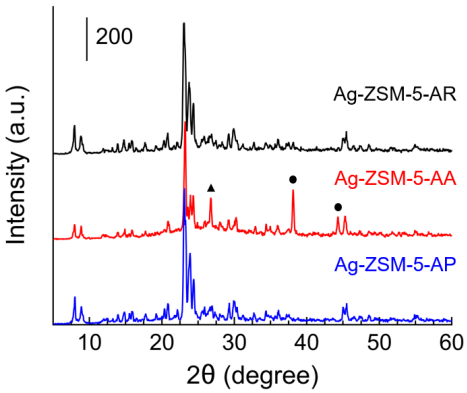

Figure 1. XRD patterns of Ag-ZSM-5-AP (blue line) and Ag-ZSM-5-AA (red line), and Ag-ZSM-5-AR with Ag/Al = 0.37. The circle and triangle indicate the diffraction peaks of Ag metal and graphene, respectively.

Figure S7 shows the XRD patterns of the H-ZSM-5-AP and Ag-ZSM-5-AP samples with various Ag/Al ratio. The XRD patterns of Ag-ZSM-5-AP with various Ag/Al ratios were consistent with those of H-ZSM-5-AP.[38] In addition, the diffraction patterns resulted from the Ag species were not observed, which supports the assumption that Ag was highly dispersed in the form of Ag^+ ions inside the zeolite pores. Moreover, the microstructure of H-ZSM-5-AP and Ag-ZSM-5-AP were analyzed from N_2 adsorption-desorption isotherms (Figure S8). The BET specific surface area (S_{BET}) and the micropore volume (V_{micro}) of Ag-ZSM-5-AP were consistent with those of H-ZSM-5-AP (Table S1). Therefore, there is no change in the pore structure of the ZSM-5 by Ag^+ ion-exchange. Figure 1 shows the XRD patterns of the Ag-ZSM-5 samples with Ag/Al = 0.37 after aromatization and regeneration. Ag-ZSM-5-AA was exhibited not only the diffraction patterns of MFI structure, but also those of Ag metal[25,39] at 38.2 and 44.4° and graphene[40,41] at 26°. These results indicate that Ag particles and highly crystalline coke

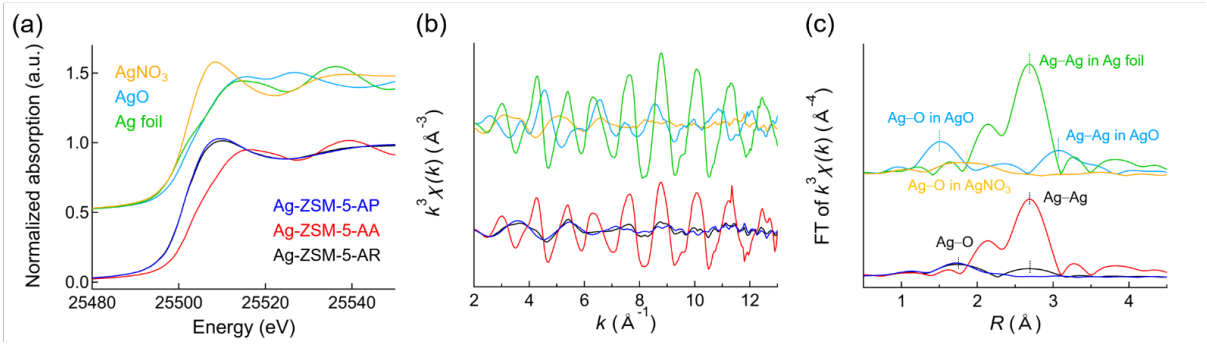

Figure 2. Ag K-edge (a) XANES, (b) k^3-weighted EXAFS, and (c) FTs of EXAFS spectra for Ag-ZSM-5-AP (blue line), Ag-ZSM-5-AA (red line), and Ag-ZSM-5-AR (black line) with Ag/Al = 0.37, together with those of the Ag foil (green line), AgO (light-blue line), and $AgNO_3$ (yellow line) as references. The FT range in k space: 3.0–11.0 $Å^{-1}$.

Table 1. Structural parameters of Ag-ZSM-5 with Ag/Al = 0.37 extracted from the EXAFS fitting for Figure 2 [a]

sample	shell	CN [b]	*r* (Å) [c]	σ^2 (Å^2) [d]	ΔE_0 (eV) [e]	*R* [f]
Ag foil	Ag–Ag	12 [f]	2.87±0.01	0.010±0.001	1.5±0.3	0.04
AgO	Ag–O	4 [f]	2.03±0.02	0.012±0.002	3.4±3.5	0.08
	Ag–Ag	12 [f]	3.27±0.02	0.019±0.001	3.4±1.7	
Ag-ZSM-5-AP	Ag–O	3.1±0.6	2.29±0.02	0.015±0.003	2.8±2.1	0.21
Ag-ZSM-5-AA	Ag–Ag	8.3±0.5	2.86±0.01	0.010±0.001	1.9±0.4	0.06
Ag-ZSM-5-AR	Ag–O	3.3±1.0	2.30±0.03	0.016±0.004	2.6±3.2	0.10
	Ag–Ag	1.5±0.6	2.88±0.02	0.013±0.003	3.3±2.9	
Ag-ZSM-5-AH	Ag–Ag	8.8±0.9	2.86±0.01	0.010±0.001	0.6±0.8	0.10
Ag-ZSM-5-O	Ag–O	1.9±0.7	2.29±0.03	0.011±0.005	0.3±4.5	0.27
	Ag–Ag	0.4±0.5	2.67±0.05	0.009±0.009	3.5±9.2	

[a] Curve fitting analyses of FTs of EXAFS were performed in *R*-space between 1.0 and 3.2 Å, and *k*-space between 3.0–11.0 Å^{-1} (in case of AgO; *R*-space between 1.0 and 4.0 Å, and *k*-space between 3.0–11.0 Å^{-1}); the amplitude reduction factor (S_0^2) was determined as 0.863 by fitting the spectrum of Ag foil; [b] Coordination number; [c] Distance of Ag–O or Ag–Ag; [d] Debye-Waller factor; [e] *R* factor (fraction of 1); [f] edge-energy shift; [g] fixed.

formed in Ag-ZSM-5 during ethylene aromatization. The crystallite size of the Ag particles as calculated by Scherrer's equation was 27.5 nm. On the other hand, the diffraction patterns of the Ag metal and graphene were no longer observed in Ag-ZSM-5-AR. The N_2 isotherms of Ag-ZSM-5-AA and Ag-ZSM-5-AR were also shown in Figure S8. The S_{BET} and the V_{micro} of Ag-ZSM-5-AA were significantly lower than those of Ag-ZSM-5-AP. Hence, the formation of coke was suggested to occlude the ZSM-5 pores. On the other hand, the S_{BET} and the V_{micro} of Ag-ZSM-5-AR were almost the same as those of Ag-ZSM-5-AP, indicating that the coke was completely removed via the regeneration process.

3.2. Chemical state and local structure of Ag species in Ag-ZSM-5 after aromatization and regeneration

The chemical state and the local structure of Ag species in Ag-ZSM-5 were investigated using *ex situ* XAFS. Ag/ZSM-5 with Ag/Al = 0.37 was typically used for *ex situ* and *in situ* XAFS. Figure 2a shows the Ag-K edge XANES spectra of Ag-ZSM-5-AP, Ag-ZSM-5-AA, and Ag-ZSM-5-AR as well as those of the reference samples (Ag foil, AgO, and $AgNO_3$). A spectral shape of Ag-ZSM-5-AP which was similar to that of $AgNO_3$ suggested that Ag species in Ag-ZSM-5-AP were present as monovalent Ag^+. Figure 2b and S9, and Table 1 show the FTs of EXAFS spectra and structural parameters determined by the EXAFS fitting, respectively. In the FTs of EXAFS spectra of Ag-ZSM-5-AP, the Ag–O scattering peak was only observed at around 1.7 Å and was different from the that in $AgNO_3$ and AgO. The EXAFS spectrum of Ag-ZSM-5-AP were best fitted the Ag–O contribution with coordination number of 3.0 and distance of 2.30. Therefore, the Ag^+ ions in Ag-ZSM-5-AP is considered to be coordinated with two O atoms in zeolite frameworks (Ag–O coordination = 2) and a water molecule (Ag–O coordination = 1).[29] The chemical states and local structure of Ag species in Ag-ZSM-5-AP obtained from *ex situ* XAFS measurement were consistent with UV-vis, IR and NH_3-TPD results. On the other hand, the XANES spectrum of Ag-ZSM-5-AA was almost identical to that of the Ag foil. In addition, only the Ag–Ag scattering peak (at 2.7 Å) was observed in the EXAFS spectrum of Ag-ZSM-5-AA, indicating that the Ag particles were formed from Ag^+ ions coordinated to the zeolite frameworks during aromatization.

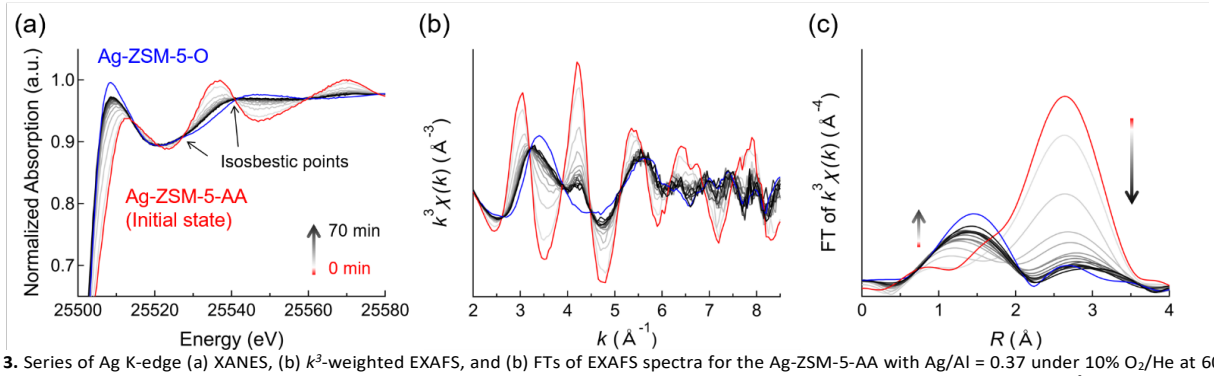

Figure 3. Series of Ag K-edge (a) XANES, (b) k^3-weighted EXAFS, and (b) FTs of EXAFS spectra for the Ag-ZSM-5-AA with Ag/Al = 0.37 under 10% O_2/He at 600 °C, together with XANES and FT of EXAFS spectra of Ag-ZSM-5-AP under 10% O_2/He at 600 °C as a reference. The FT range in *k* space: 3.0–7.0 Å^{-1}.

The formation of Ag particles during aromatization was in accordance with the XRD results. Assuming an Ag particle with a truncated octahedral structure, the Ag particle size was estimated from the Ag–Ag coordination number of 8.3 to be approximately 1.5 nm (Figure S10).[42,43] There is a large gap between the Ag particle sizes estimated from XRD and XAFS. The Ag particle size may be overestimated because XRD is sensitive to large crystalline Ag particles. On the other hand, the Ag particle size is likely underestimated because XAFS is estimated from the average Ag−Ag coordination number of Ag species. However, it is important that both Ag particle sizes were larger than the pore size (approximately 0.6 nm) of the 10-membered ring of ZSM-5.[29,44] These results can conclude that Ag particles were mainly located outside the zeolite pore. The XANES and FTs of EXAFS spectra of Ag-ZSM-5-AR were almost consistent with Ag-ZSM-5-AP. Therefore, the regeneration treatment caused the redispersion of Ag particles inside the ZSM-5 pore in the form of Ag^+ ions. However, in addition to the Ag–O scattering peak, a weak Ag–Ag scattering peak was found around 2.7 Å. This suggests that some Ag particles remain without redispersion in the form of Ag^+ ions.

3.3. Redispersion behavior of Ag particles into ZSM-5 in the presence of coke

The redispersion behavior of Ag particles during the regeneration process was observed by *in situ* XAFS. Figure 3a shows the Ag K-edge XANES spectra for Ag-ZSM-5-AA under 10% O_2/He at 600 °C. The increase in the white line intensity around 25508 eV was caused by the oxidation of Ag^0 to Ag^+. However, even after 70 min of regeneration, the spectrum of Ag-ZSM-5 did not fully recover to that of Ag-ZSM-5-AP. This indicates that some Ag particles remained on the surface of ZSM-5 without redispersion into Ag^+ ions. Figure 3b shows the dynamics of FTs of EXAFS spectra under 10% O_2/He at 600 °C. After O_2 injection, the intensity of the scattering peak of Ag−Ag (at 2.6 Å) gradually decreased while that of Ag−O (at 1.6 Å) increased.

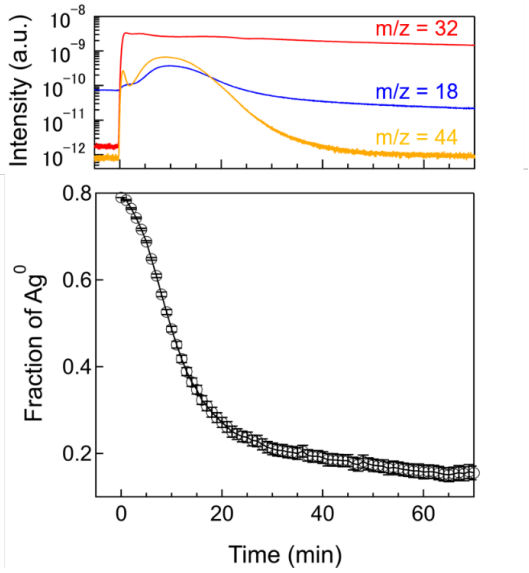

Figure 4. The outlet concentrations detected by mass spectroscopy (top) and time course of Ag^0 fraction determined by LCF for a series of Ag K-edge XANES spectra measured at 600 °C under 10% O_2/Ar (bottom).

These results indicated that the Ag particles were redispersed to Ag^+ ions under the O_2 atmosphere.

LCF of *in situ* XANES spectra was performed in the range of 25480–25530 eV to quantify the fraction of Ag^+ and Ag^0. The fractions of Ag^0 in Ag-ZSM-5-AP and Ag foil were assumed as 0 and 1, respectively. Based on UV-vis and XAFS spectroscopy, Ag species in the Ag-ZSM-5-AP were assigned to only isolated Ag^+ ions (Figure 2 and S4). The fractions of Ag^0 in Ag-ZSM-5-O and Ag-ZSM-5-AA used as standard samples of *in situ* XANES spectra, were estimated as 0.12 and 0.79, respectively (Figure S11). In Ag-ZSM-5-O, some Ag ions were self-reduced by heat at 600 °C even under oxygen atmosphere (Table 1 and Figure S12). In addition, the decrease in Ag−O coordination number can be explained by the desorption of water from Ag^+ ions coordinated with zeolite frameworks. Examples of LCF of *in situ* XANES spectra were shown in Figure S13. The fractions of Ag^0 in Ag-ZSM-5 were plotted against time (lower graph in Figure 4). According to the above EXAFS results, the decrease in the Ag^0 fraction indicated the redispersion of Ag particles (Figure 3b). The redispersion behavior of Ag particles was obtained as a sigmoid-like curve instead of a simple exponential curve. A slow Ag particle redispersion was observed at the beginning of the O_2 introduction (0–5 min) followed by an accelerated redispersion within 5–20 min. After 20 min of the O_2 introduction, when the Ag particle redispersion reached about 70%, the redispersion slowed down and almost stopped after 70 min. The top graph in Figure 4 shows the gas concentration at the outlet as detected by the mass spectrometer. CO_2 (m/z = 44) and H_2O (m/z = 18) generated by coke combustion were detected immediately after the introduction of O_2 (m/z = 32). Therefore, the coke combustion simultaneously proceeded along with the redispersion of Ag particles under the O_2 atmosphere. Finally, CO_2 production almost stopped after 40 min, indicating that Ag redispersion and coke combustion proceeded on a similar time scale at 600 °C. In addition, hydrocarbons- and hydrogen-derived H_2O in the coke possibly caused dealumination of zeolite. The constant O_2 (m/z = 32) concentration measured during regeneration process indicated that O_2 was sufficient for the redispersion of Ag particles. Effect of coke on Ag particle redispersion was investigated using the Ag particles on ZSM-5 without coke (Ag-ZSM-5-AH) prepared by H_2 reduction at 600°C. XANES, EXAFS spectra, and structural parameters of Ag-ZSM-5-AH similar to those of Ag-ZSM-5-AA (Figure S9 and S12, and Table 1). The redispersion of Ag particles in the absence of coke was obtained as an exponential-like curve (Figure S14). Thus, the slow redispersion of Ag particles may be attributed to partial coke deposition on Ag particles and in ZSM-5 pores. However, the dispersion of Ag particles was accelerated immediately after 5 min of the O_2 introduction (Figure 4). On the other hand, the redispersion of Ag particles in the presence and absence of coke clearly slows down after reaching about 70%. This suggests that the diffusion of Ag^+ ions into the ZSM-5 pores is a rate-limiting step.

The redispersion behavior of Ag particles into ZSM-5 in the presence of coke was measured at various temperatures (450–600 °C) (Figures 5a and S15). The rate of Ag redispersion decreased with the decrease in temperature. The Ag^0 fraction

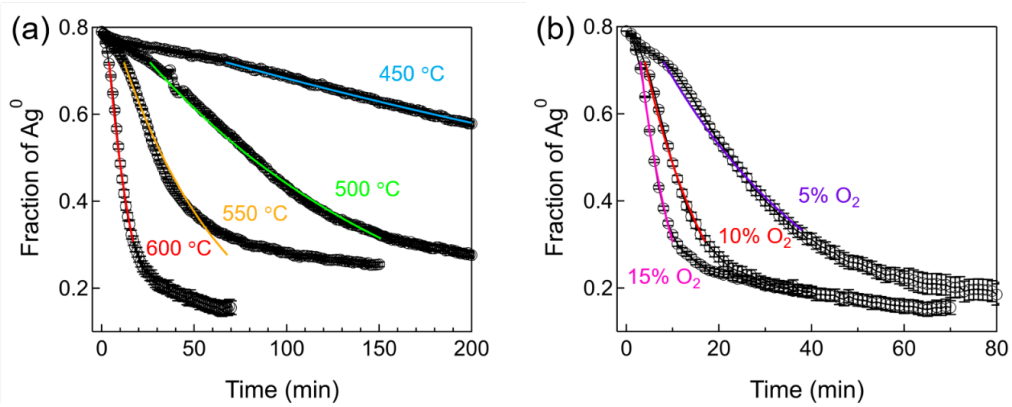

Figure 5. Ag^0 fraction calculated by LCF for a series of Ag K-edge XANES spectra measured at (a) various temperatures under 10% O_2/Ar and (b) 600 °C under various O_2 concentrations. Colored lines indicate the fitting results obtained using a pseudo-first-order kinetic model.

within the range of 0.3–0.7 was fitted by using the following pseudo-first-order kinetic model (i.e., simple exponential model) to estimate the rate constant for the redispersion of Ag particles.[45–47]

$$[Ag^0]_t = [Ag^0]_i \times \exp\{-k_1(t - t_{offset})\} \quad (1)$$

where $[Ag^0]_t$ is the fraction of Ag^0 at time t, $[Ag^0]_i$ is the fraction of Ag^0 at the initial state in the fitting range ($= 0.7$), k_1 is the rate constant of Ag particle redispersion, and t_{offset} is the time offset corresponding to the time t for $[Ag^0]_i$. The t_{offset} was introduced to analyze the Ag redispersion rate using the simple pseudo-first-order kinetic model.

The rate constant of Ag redispersion at 600 °C was found to be 41.1, 10.0, and 3.8 times higher than those at 450, 500, and 550 °C, respectively (Table S2). The presence of coke hardly affected the rate constant of redispersion (Table S3). In addition, O_2 concentration is possible to be important parameter of the regeneration process for Ag-ZSM-5. Therefore, the effect of O_2 concentration on the rate of Ag particle redispersion was investigated. Figures 5b and S16 show the redispersion behavior of Ag particles measured under various O_2 concentrations. The rate of the Ag particle redispersion increased with increasing the O_2 concentration from 5% to 15%. The rate constants of redispersion under 15% O_2/He was 4.8 and 1.9 times higher than those under 5% and 10% O_2/He, respectively (Table S2). The positive dependence of the rate constants on the O_2 concentration suggests that the O_2 activation on Ag particles is an important factor for the redispersion to Ag$^+$ ions.

3.4. Combustion behavior of coke over Ag-ZSM-5

The combustion behavior of coke deposited during ethylene aromatization on Ag-ZSM-5 was analyzed using TGA. The Ag-ZSM-5 sample weights before the introduction of O_2 and after complete coke combustion were assumed to be the coke deposition of 1 (full) and 0 (none), respectively. The coke deposition in H-ZSM-5 and Ag-ZSM-5 after ethylene aromatization was 12.2 and 10.9 wt%, respectively. The combustion behavior in Ag-ZSM-5 was little different from that in H-ZSM-5, which indicates that the Ag particles or Ag$^+$ ions in Ag-ZSM-5 were either less active for coke combustion or in poor contact with coke particles (Figure S17). Figure 6a shows the coke combustion behavior measured at various temperatures. The coke combustion rate significantly increased with the temperature. At <500 °C, the coke combustion was extremely slow and more than 90% of the coke remained after 200 min of regeneration (Figure S18). The significant decrease in coke combustion rates at <500 °C reflects the presence of coke species with different combustion characteristics. Coke includes a highly crystalline graphite structure “hard coke” and its precursors “soft coke”, which are cyclic compounds, such as naphthalene and anthracene.[10,11,48,49] The graphite structure is formed by the condensation of cyclic compounds. Figure S19 shows Raman spectra of Ag-ZSM-5-AA and -AR450 (after

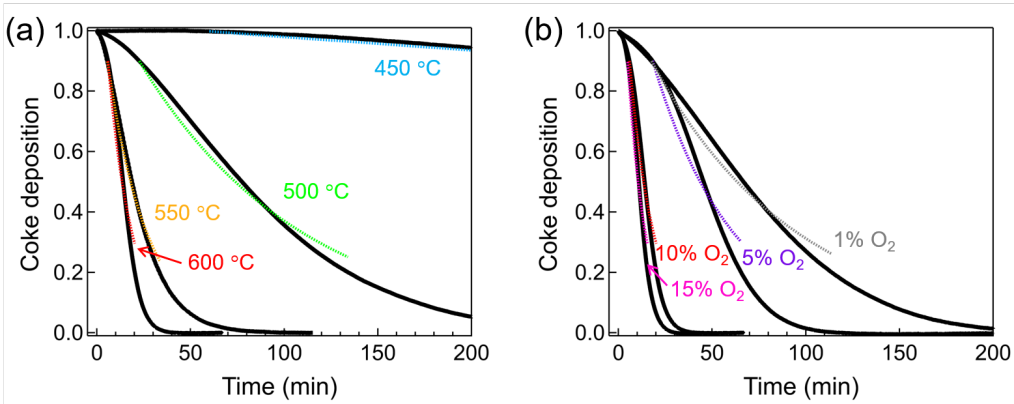

Figure 6. Behaviors of coke combustion in Ag-ZSM-5-AA with Ag/Al = 0.37 measured at (a) various temperatures under 10% O_2/Ar, and (b) 600 °C under various O_2 concentrations. Colored lines indicate the fitting results by pseudo-first-order kinetic model.

regeneration at 450°C). After regeneration at 450°C, Intensity of Raman peaks at 1377 and 1610 cm^{-1} were decreased. The Raman peaks at 1377 and 1610 cm^{-1} were derived from C=C stretching and aromatic ring breathing vibrations of the cyclic compounds, respectively (Table S4).[10,11,49] Therefore, it can be concluded that only the combustion of soft coke was observed at <500 °C, while hard coke burned at ≥500 °C.[41]

Figure 6b shows the combustion behavior of coke in Ag-ZSM-5 at 600 °C under various O_2 concentration. Similar to the redispersion of Ag particles, the coke combustion rate slowed with the decrease in O_2 concentration. However, even under 1% O_2 atmosphere, a complete combustion of coke in Ag-ZSM-5 was achieved after 200 min. Moreover, the coke deposition within the range of 0.2–0.9 was fitted using the following pseudo-first-order kinetic model to estimate the rate constant for the coke combustion in Ag-ZSM-5.

$$[coke]_t = [coke]_i \times \exp\{-k_2(t - t_{offset})\} \qquad (2)$$

where $[coke]_t$ is the coke deposition at time t, $[coke]_i$ is the coke deposition at the initial state in the fitting range ($= 0.9$), k_2 is the rate constant of coke combustion, and t_{offset} is the time offset which corresponds to time t for $[coke]_i$. Exceptionally, for samples measured at 400 and 450 °C, the t_{offset} was set to 60 min.

The rate constant of coke combustion at 600 °C was 260, 156, 6.8, and 1.6 times higher than those at 400, 450, 500, and 550 °C, respectively (Table S5). On the other hand, the rate constant of coke combustion under 15% O_2/He was 8.2, 4.5, and 1.4 times higher than those under 1%, 5%, and 10% O_2/He.

3.5. Comparison between the rate constants of Ag particle redispersion and coke combustion

Figure 7a shows the temperature dependence of the rate constants of Ag particle redispersion k_1 and coke combustion k_2. The k_1/k_2 ratio was also plotted against temperature (Figure 7b). At ≥500 °C, k_1 was smaller to k_2 as the k_1/k_2 ratio was close to 0.5, suggesting that the coke combustion proceeded slightly faster than Ag redispersion on ZSM-5. At <500 °C, k_1 was larger than k_2. At 450 °C, the k_1/k_2 ratio was about 3, suggesting that the redispersion of Ag particles on ZSM-5 preferentially proceeded over coke combustion. Figure 7c shows the dependence of the rate constants k_1 and k_2 on the O_2 concentration. Both k_1 and k_2 increased with the O_2 concentration. However, the k_1/k_2 ratio was almost independent of the O_2 concentration (Figure 7d).

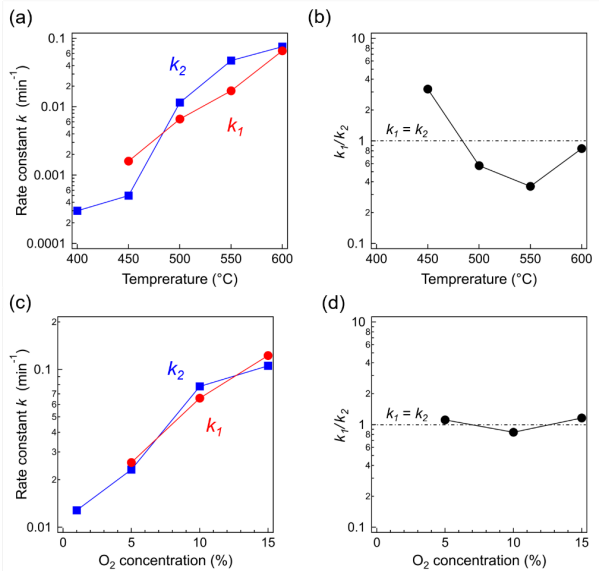

Figure 7. Dependence of the rate constant of Ag^0 redispersion (k_1) and coke combustion (k_2) on (a) temperature and (c) O_2 concentration. Plots of k_1/k_2 ratio against (b) temperature and (d) O_2 concentration.

3.6. Hydrothermal stability of Ag-ZSM-5

As mentioned, the dealumination of zeolites is caused by H_2O generated during the combustion of coke that includes hydrocarbons and hydrogen. Ag^+ ion exchange in zeolites is expected to inhibit its dealumination, since the dealumination begins with an H_2O attack on the H^+ (Brønsted acid) site in the zeolites. The effect of the Ag^+ ions in the ZSM-5 on the dealumination of ZSM-5 under hydrothermal conditions was investigated using ^{27}Al MAS NMR. The ^{27}Al MAS NMR spectra of H-ZSM-5-AP and Ag-ZSM-5-AP exhibited strong and weak signals around 55 and 0 ppm, which were attributed to the four- and six-coordinate Al^{3+} sites, respectively, (Figure S20).[21,31,50,51] The four-coordinate Al^{3+} species are incorporated into the

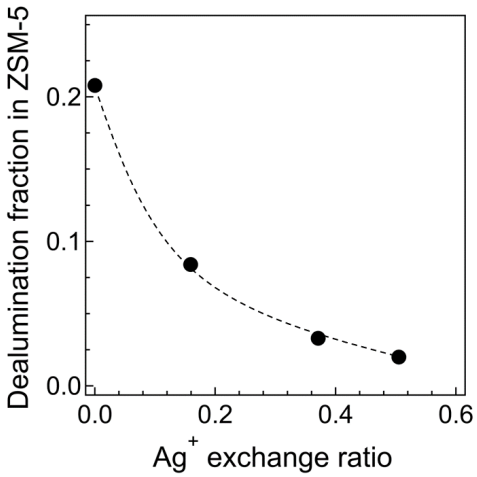

Figure 8. Dependence of Ag^+ exchange ratio on the dealumination fraction in ZSM-5.

Scheme 1. Schematic representation of temperature dependence of redispersion of Ag particles into ZSM-5, and coke combustion.

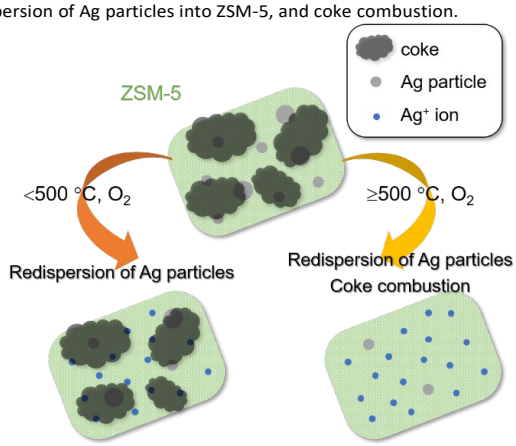

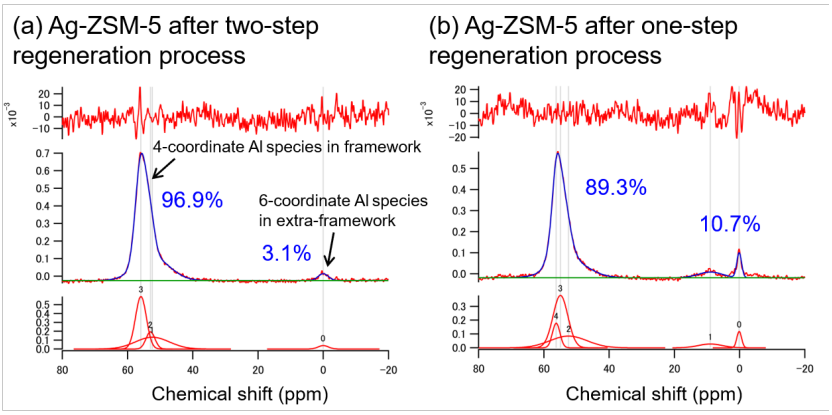

Figure 9. (middle) ^{27}Al MAS NMR spectra of Ag-ZSM-5 (Ag/Al = 0.37) after (a) two-step and (b) one-step regeneration process, together with Gaussian fitting results. (top) fitting error and (bottom) each fitted Gaussian peak. Asymmetric NMR peaks were fitted using two or more Gaussian peaks because ^{27}Al have quadrupole moment and Al atoms in ZSM-5 were slightly different. In the case of two-step regeneration process, Ag-ZSM-5-AA was treated under 10% O_2/Ar at 450 °C for 9 h and then heated to 700 °C for 1 h. In the case of one-step regeneration process, Ag-ZSM-5-AA was treated under 10% O_2/Ar at 700 °C for 1 h. These aromatization–regeneration cycles were repeated three times.

zeolite framework in the form of a bridged Si–OH–Al. On the other hand, the six-coordinate Al^{3+} species is attributed to the extra-framework Al atoms. The NMR spectrum of Ag-ZSM-5-AP was consistent with that of H-ZSM-5-AP. Therefore, the coordination environment of Al in the ZSM-5 hardly changed by Ag^+ ion exchange. To investigate the hydrothermal stability of zeolites, H-ZSM-5 and Ag-ZSM-5 with various Ag/Al ratios were treated under hydrothermal conditions (at 700 °C and under 3% H_2O/N_2) for 16 h (denoted H-ZSM-5-HT and Ag-ZSM-5-HT, respectively). H-ZSM-5-HT showed a decrease in the NMR peak intensity at 55 ppm and an increase at 0 ppm (Figure S21). In addition, a new peak appeared around 30 ppm, which was attributed to the five-coordinate Al^{3+} sites, which represent extra-framework Al atoms.[31,50,51] These results indicated that the Al atoms were moved from the zeolite frameworks to the extra-frameworks under the hydrothermal treatment. According to NH_3-TPD, H-MFI-HT showed a decrease in the desorption peak of NH_3 from the H^+ site (Figure S22). On the other hand, no five-coordinate Al species were observed in Ag-ZSM-5, even after the hydrothermal treatment. Furthermore, in Ag-ZSM-5-HT, the peak intensity of the six-coordinate Al^{3+} species decreased with the increase in the Ag/Al ratio. The dealumination fraction in ZSM-5 was quantified based on the peak area of each Al species in the NMR spectra. The fraction of dealumination in Ag-ZSM-5-HT decreased with the increase in the Ag/Al ratio (Figure 8). Therefore, it was inferred that the dealumination was suppressed by the ion exchange of H^+ with Ag^+ in ZSM-5. On the other hand, NH_3-TPD profile of Ag-ZSM-5-AH indicated that the H^+ sites in the ZSM-5 were formed simultaneously with the formation of Ag particles (Figure S23). Therefore, the Ag-ZSM-5 which contains Ag particles, would cause dealumination due to the abundance of H^+ sites. From the above results, it can be concluded that to prolong the catalyst lifetime, the Ag redispersion should be promoted over coke combustion during the regeneration process.

Scheme 1 summarizes the temperature dependence of Ag particle redispersion and coke combustion in Ag-ZSM-5. At <500 °C, Ag particles slowly redispersed into the ZSM-5 pore, while coke combustion hardly occurred. At ≥500 °C, the redispersion of Ag particles and coke combustion proceeded simultaneously and coke combustion was especially rapid. In addition, the rapid coke combustion, which generates water vapor, can cause the dealumination of ZSM-5. This particularly occurred when Ag^+ ions were absent at the ion-exchange site in ZSM-5. Therefore, we recommend an optimal two-step regeneration of Ag-ZSM-5 for ethylene aromatization, in which the redispersion of Ag particles proceed at temperatures lower than 500 °C followed by coke combustion at temperatures above 500 °C. The two-step regeneration process is expected to extend the Ag-ZSM-5 catalyst life for ethylene aromatization. Figure 9 shows the ^{27}Al MAS NMR spectra of Ag-ZSM-5 catalysts treated by the two-step and one-step regeneration processes. The dealumination fraction of Ag-ZSM-5 after two-step regeneration process was the same as that of Ag-ZSM-5-AP (ca. 3%). Therefore, the dealumination in Ag-ZSM-5 did not occur during the two-step regeneration process. On the other hand, in Ag-ZSM-5 regenerated by 1-step process, the extra-framework Al species, which were produced by the dealumination, increased to 10%. These results demonstrated that the two-step regeneration process was more superior in terms of suppressing the dealumination of Ag-ZSM-5 than the one-step regeneration process.

4. Conclusions

In this study, the redispersion of Ag particles to Ag^+ ions in the presence of coke was observed using *in situ* Ag K-edge XAFS spectroscopy. The redispersion behavior of Ag particles was revealed by LCF analysis of the Ag K-edge XANES spectra, and the rate constants of Ag particle redispersion were studied using a pseudo-first-order kinetic model. In addition, the combustion behavior of coke on Ag-ZSM-5 was analyzed using TGA. The rate constants of Ag particle redispersion and coke combustion were found to be strongly dependent on temperature. At ≥500 °C, the relative rate constants of Ag redispersion and coke combustion (k_1/k_2) was close to 0.5, indicating that the coke combustion faster than Ag redispersion which proceeded simultaneously. However, at <500 °C, Ag redispersion proceeded preferentially over coke combustion

(k_1/k_2≈3). The rate constants of Ag redispersion and coke combustion were found to increase with the increase in the oxygen concentration. However, the oxygen concentration hardly affected the k_1/k_2 ratio. Based on the above results, a two-step regeneration process for Ag-ZSM-5 was proposed to extend the lifetime of the catalyst. In the first step, Ag particles are converted into Ag^+ ions and redispersed inside the ZSM-5 pore by exposure to an O_2 atmosphere at low temperature (<500 °C). The Ag^+ ions in the ZSM-5 pore suppress the H_2O-induced dealumination, which occurs during coke combustion. In the second step, the coke is completely combusted at high temperature (≥500 °C) and the Ag redispersion is completed.

5. Conflicts of interest

There are no conflicts to declare.

6. Acknowledgements

This work was partly supported by the JSPS KAKENHI Grant-in-Aids for Scientific Research (B) (Grant Nos. 18H01787) and JSPS Fellows (Grant Nos. 19J15440) from the Ministry of Education, Culture, Sports, Science and Technology (MEXT), Japan. A part of this work was managed by the Elements Strategy Initiative for Catalysts & Batteries (ESICB, JPMXP0112101003), which is also supported by MEXT. XAFS measurement was conducted at BL14B2 of SPring-8 (Approval No. 2018A1797, 2018B1806, and 2019A1710). The authors thank Dr. Hiroyuki Asakura (Kyoto Univ.) and Dr. Takeshi Watanabe (Japan Synchrotron Radiation Research Institute (JASRI)), Dr. Hironori Ofuchi (JASRI) for XAFS measurement. ^{27}Al MAS NMR measurement was performed at Research Center for Materials Science (RCMS), Nagoya University. The authors thank Dr. Yutaka Maeda (Nagoya Univ.) for the NMR measurement.

7. References

1 H. Wang, Y. Hou, W. Sun, Q. Hu, H. Xiong, T. Wang, B. Yan and W. Qian, *ACS Catal.*, 2020, **10**, 5288–5298.

2 M. Guisnet, N. S. Gnep and F. Alario, *Appl. Catal. A, Gen.*, 1992, **89**, 1–30.

3 S. Nayak, Vikram and V. R. Choudhary, *Appl. Catal.*, 1984, **9**, 251–261.

4 W. Liu, W. Wang, K. Tang, J. Guo, Y. Ren, S. Wang, L. Feng and Y. Yang, *Catal. Sci. Technol.*, 2020, **10**, 2774–2785.

5 H. Coqueblin, A. Richard, D. Uzio, L. Pinard, Y. Pouilloux and F. Epron, *Catal. Today*, 2017, **289**, 62–69.

6 V. R. Choudhary, P. Devadas, S. Banerjee and A. K. Kinage, *Microporous Mesoporous Mater.*, 2001, **47**, 253–267.

7 X. Chen, M. Dong, X. Niu, K. Wang, G. Chen, W. Fan, J. Wang and Z. Qin, *Chinese J. Catal.*, 2015, **36**, 880–888.

8 M. F. Hsieh, Y. Zhou, H. Thirumalai, L. C. Grabow and J. D. Rimer, *ChemCatChem*, 2017, **9**, 1675–1682.

9 N. Kosinov, E. A. Uslamin, L. Meng, A. Parastaev, Y. Liu and E. J. M. Hensen, *Angew. Chem. Int. Ed.*, 2019, 7068–7072.

10 H. An, F. Zhang, Z. Guan, X. Liu, F. Fan and C. Li, *ACS Catal.*, 2018, **8**, 9207–9215.

11 P. M. Allotta and P. C. Stair, *ACS Catal.*, 2012, **2**, 2424–2432.

12 E. T. C. Vogt and B. M. Weckhuysen, *Chem. Soc. Rev.*, 2015, **44**, 7342–7370.

13 Y. Nakasaka, T. Tago, H. Konno, A. Okabe and T. Masuda, *Chem. Eng. J.*, 2012, **207**–**208**, 368–376.

14 M. Nielsen, A. Hafreager, R. Y. Brogaard, K. De Wispelaere, H. Falsig, P. Beato, V. Van Speybroeck and S. Svelle, *Catal. Sci. Technol.*, 2019, **9**, 3721–3725.

15 T. Sano, H. Ikeya, T. Kasuno, Z. B. Wang, Y. Kawakami and K. Soga, *Zeolites*, 1997, **19**, 80–86.

16 M. C. Silaghi, C. Chizallet, E. Petracovschi, T. Kerber, J. Sauer and P. Raybaud, *ACS Catal.*, 2015, **5**, 11–15.

17 K. Stanciakova, B. Ensing, F. Göltl, R. E. Bulo and B. M. Weckhuysen, *ACS Catal.*, 2019, **9**, 5119–5135.

18 A. W. Petrov, D. Ferri, O. Krö and J. A. Van Bokhoven, *ACS Catal.*, 2019, **9**, 2303–2312.

19 T. Usui, Z. Liu, S. Ibe, J. Zhu, C. Anand, H. Igarashi, N. Onaya, Y. Sasaki, Y. Shiramata, T. Kusamoto and T. Wakihara, *ACS Catal.*, 2018, 9162–9173.

20 Y. Cui, Y. Wang, D. Mei, E. D. Walter, N. M. Washton, J. D. Holladay, Y. Wang, J. Szanyi, C. H. F. Peden and F. Gao, *J. Catal.*, 2019, **378**, 363–375.

21 X. He, X. Huang, Z. Wang and Y. Yan, *Microporous Mesoporous Mater.*, 2011, **142**, 398–403.

22 Y. Ono and T. Baba, *Phys. Chem. Chem. Phys.*, 2015, **17**, 15637–15654.

23 K. I. Shimizu, K. Sugino, K. Kato, S. Yokota, K. Okumura and A. Satsuma, *J. Phys. Chem. C*, 2007, **111**, 1683–1688.

24 J. Shibata, K. I. Shimizu, Y. Takada, A. Shichi, H. Yoshida, S. Satokawa, A. Satsuma and T. Hattori, *J. Catal.*, 2004, **227**, 367–374.

25 Z. Huang, J. Zhang, Y. Du, Y. Zhang, X. Wu and G. Jing, *ChemCatChem*, 2019, 561–568.

26 Y. Gao, X. Wu, S. Liu, M. Ogura, M. Liu and D. Weng, *Catal. Sci. Technol.*, 2017, **7**, 3524–3530.

27 Z. Huang, X. Gu, Q. Cao, P. Hu, J. Hao, J. Li and X. Tang, *Angew. Chem. Int. Ed.*, 2012, **51**, 4198–4203.

28 B. Ravel and M. Newville, *J. Synchrotron Radiat.*, 2005, **12**, 537–541.

29 T. Yumura, A. Oda, H. Torigoe, A. Itadani, Y. Kuroda, T. Wakasugi and H. Kobayashi, *J. Phys. Chem. C*, 2014, **118**, 23874–23887.

30 W.-S. Ju, M. Matsuoka, K. Iino, H. Yamashita and M. Anpo, *J. Phys. Chem. B*, 2004, **108**, 2128–2133.

31 Z. Wang, L. A. O'Dell, X. Zeng, C. Liu, S. Zhao, W. Zhang, M. Gaborieau, Y. Jiang and J. Huang, *Angew. Chem. Int. Ed.*, 2019, **58**, 18061–18068.

32 C. Kalamaras, D. Palomas, R. Bos, A. Horton, M. Crimmin and K. Hellgardt, *Catal. Lett.*, 2016, **146**, 483–492.

33 S. Brandenberger, O. Kröcher, A. Wokaun, A. Tissler and R. Althoff, *J. Catal.*, 2009, **268**, 297–306.

34 F. Benaliouche, Y. Boucheffa, P. Ayrault, S. Mignard and P. Magnoux, *Microporous Mesoporous Mater.*, 2008, **111**, 80–88.

35 Y. W. Zhao, B. X. Shen and H. Sun, *RSC Adv.*, 2016, **6**, 93086–93093.

36 Y. Chen, K. Gong, F. Jiao, X. Pan, G. Hou, R. Si and X. Bao, *Angew. Chem. Int. Ed.*, 2020, **59**, 6529–6534.

37 G. Qi, Q. Wang, J. Xu, J. Trébosc, O. Lafon, C. Wang, J. P. Amoureux and F. Deng, *Angew. Chem. Int. Ed.*, 2016, **55**, 15826–15830.

38 H. Yang, C. Ma, X. Zhang, Y. Li, J. Cheng and Z. Hao, *ACS Catal.*, 2018, **8**, 1248–1258.

39 F. Wang, J. Ma, G. He, M. Chen, C. Zhang and H. He, *ACS Catal.*, 2018, **8**, 2670–2682.

40 A. Sayah, F. Habelhames, A. Bahloul, B. Nessark, Y. Bonnassieux, D. Tendelier and M. El Jouad, *J. Electroanal. Chem.*, 2018, **818**, 26–34.

41 L. Pahalagedara, H. Sharma, C. H. Kuo, S. Dharmarathna, A. Joshi, S. L. Suib and A. B. Mhadeshwar, *Energy and Fuels*, 2012, **26**, 6757–6764.

42 D. Guillemot, M. Polisset-Thfoin, J. Fraissard and D. Bonnin, *J. Phys. Chem. B*, 2002, **101**, 8243–8249.

43 R. E. Benfield, *J. Chem. Soc. Faraday Trans.*, 1992, **88**, 1107–1110.

44 T. Yumura, T. Nanba, H. Torigoe, Y. Kuroda and H. Kobayashi, *Inorg. Chem.*, 2011, **50**, 6533–6542.

45 H. Asakura, S. Hosokawa, T. Ina, K. Kato, K. Nitta, K. Uera, T. Uruga, H. Miura, T. Shishido, J. Ohyama, A. Satsuma, K. Sato, A. Yamamoto, S. Hinokuma, H. Yoshida, M. Machida, S. Yamazoe, T. Tsukuda, K. Teramura and T. Tanaka, *J. Am. Chem. Soc.*, 2018, **140**, 176–184.

46 M. Harada and Y. Inada, *Langmuir*, 2009, **25**, 6049–6061.

47 H. Asakura, K. Teramura, T. Shishido, T. Tanaka, N. Yan, C. Xiao, S. Yao and Y. Kou, *Phys. Chem. Chem. Phys.*, 2012, **14**, 2983.

48 N. Chaouati, A. Soualah, M. Chater, M. Tarighi and L. Pinard, *J. Catal.*, 2016, **344**, 354–364.

49 Y. T. Chua and P. C. Stair, 2003, **213**, 39–46.

50 J. Kanellopoulos, A. Unger, W. Schwieger and D. Freude, *J. Catal.*, 2006, **237**, 416–425.

51 M. C. Silaghi, C. Chizallet and P. Raybaud, *Microporous Mesoporous Mater.*, 2014, **191**, 82–96.